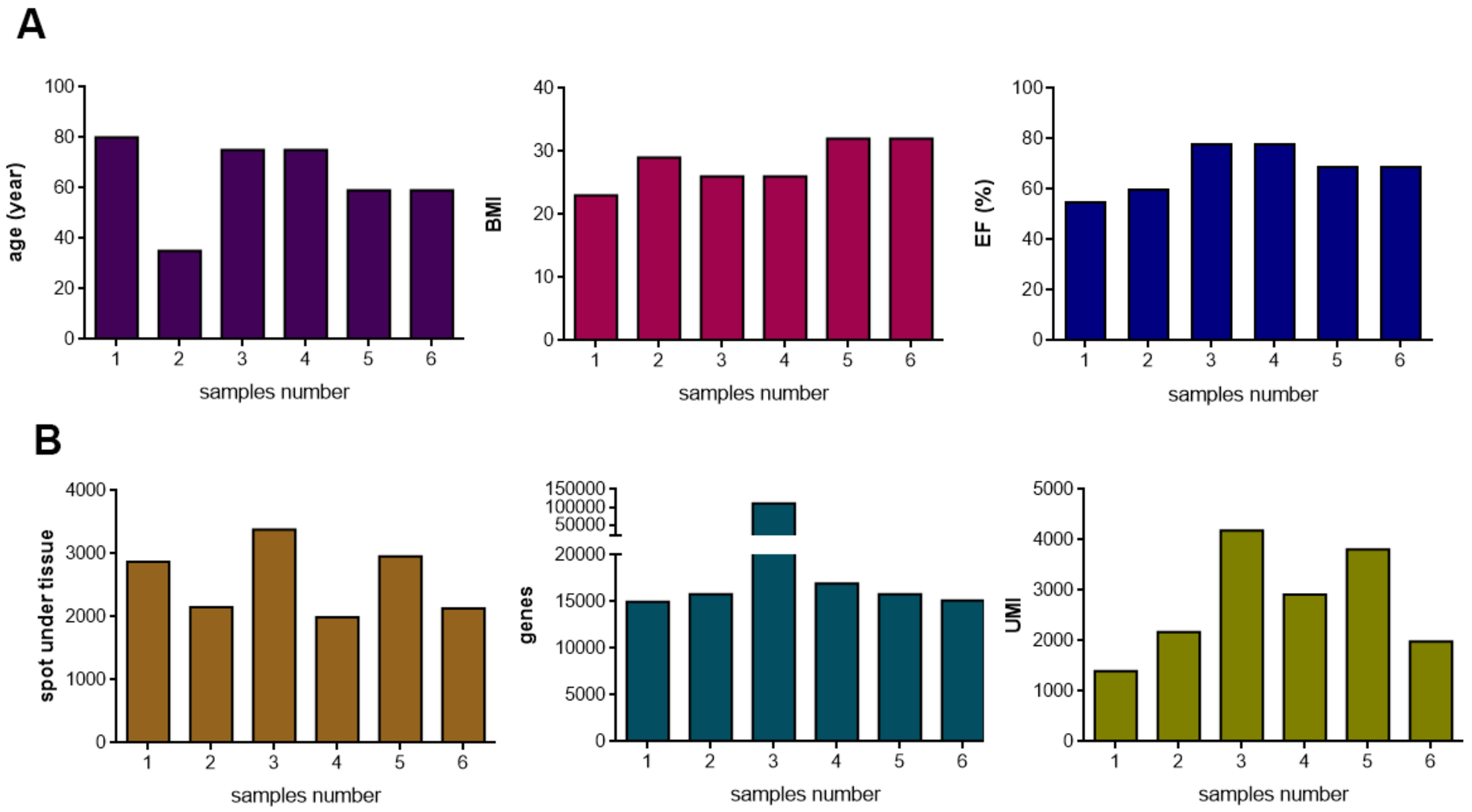

fig. S1 Characteristics of human right atria samples. (**A**) Histograms represent age, body mass index (BMI) and left ventricular ejection fraction (EF) for the 6 human right atria samples used for Vision Gene Expression. (**B**) Histograms represent count of spots, genes and unique molecular identifier (UMI) for each 6 human right atria samples.

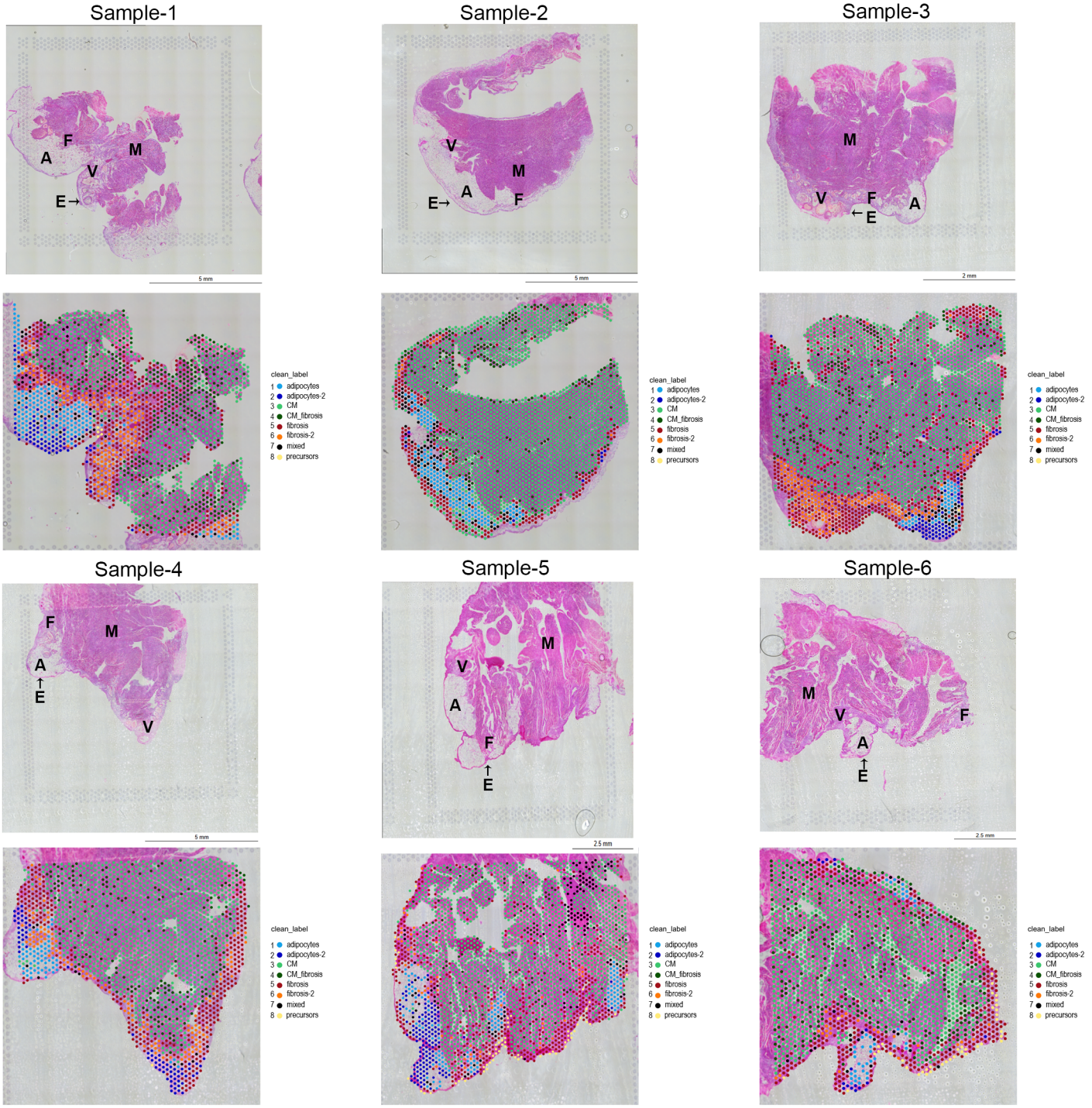

fig. S2 Spatial transcriptomic of human atrial specimens reveals various component in the subepicardium. Spatial transcriptomic performed on Formalin-Fixed Paraffin-Embedded (FFPE) human right atrial specimens (n=6) with a fatty-to-fibrosis component. Five-µm section of human atrial tissue after H&E staining (up) associated with spot plot clusters identified using Seurat based on specific gene expression. Scale bar: 2 to 5 mm.
A, adipocytes; M, myocardium; V, vessels; F, fibrosis; E, epicardium (arrow).

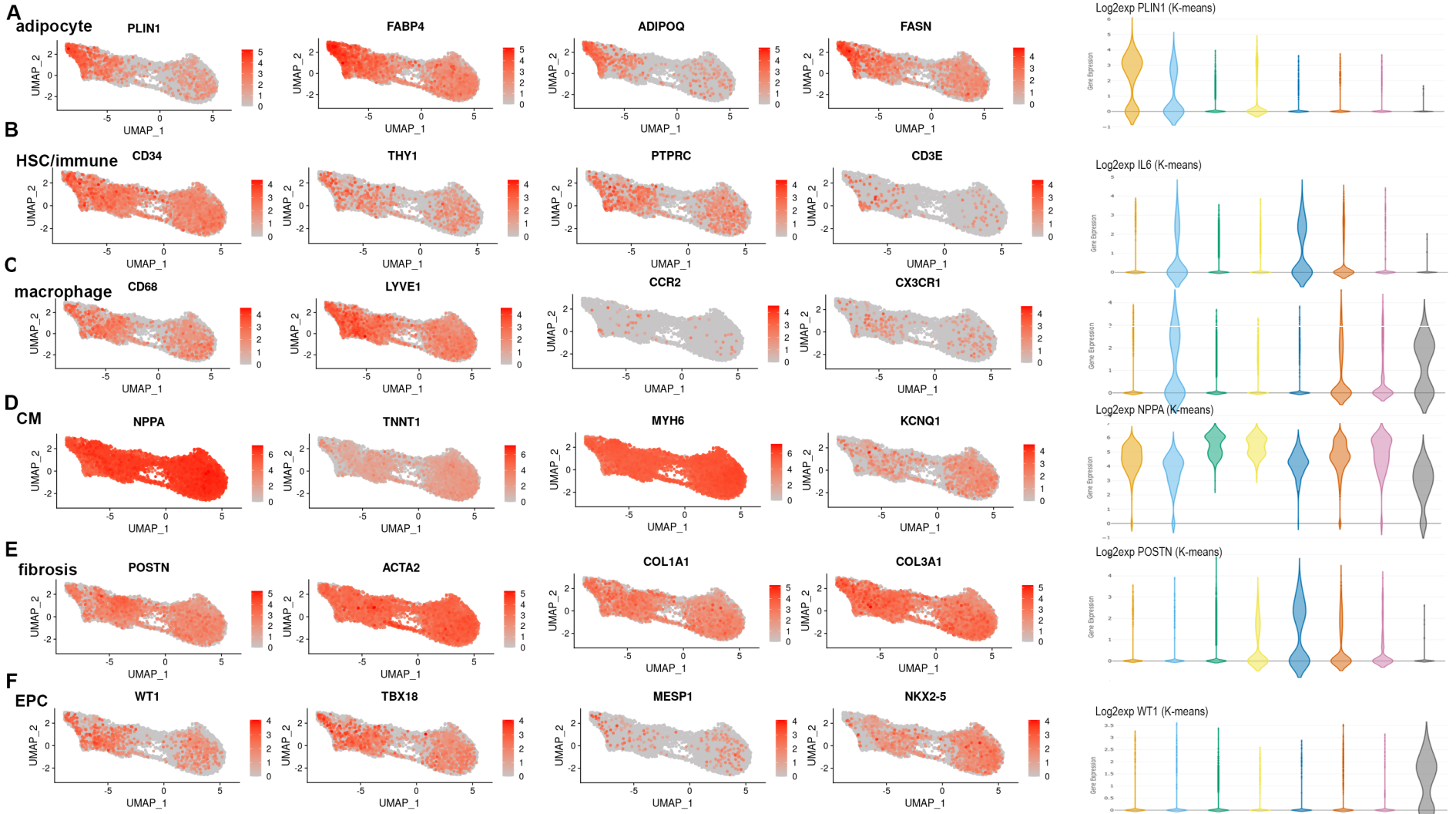

fig. S3 Spatial transcriptomic of human atrial specimens merged reveals gene expression patterns. Uniform manifold approximation and projection (UMAP) clustering with Seurat showing gene expression patterns for human atrial specimens merged. Violin plots showing the gene expression levels (normalized log-transformed values) according to the clusters.

fig. S4 Spatial transcriptomic of human atrial specimens reveals inflammation signature. Uniform manifold approximation and projection (UMAP) clustering with Seurat showing gene expression patterns for the 6 samples merged showing immune cells (**A**) and inflammation (**B**) patterns.

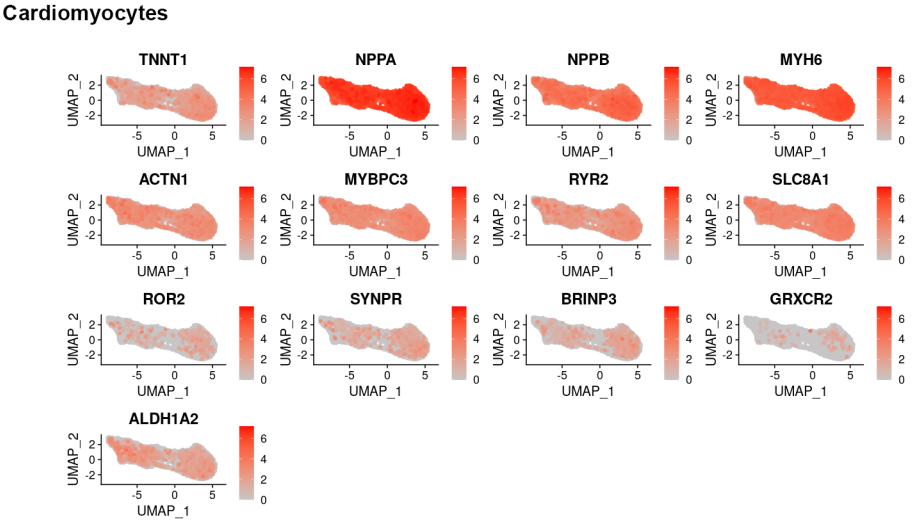

fig. S5 Spatial transcriptomic of human atrial specimens reveals cardiomyocyte signature. Uniform manifold approximation and projection (UMAP) clustering with Seurat showing gene expression patterns for 6 samples merged.

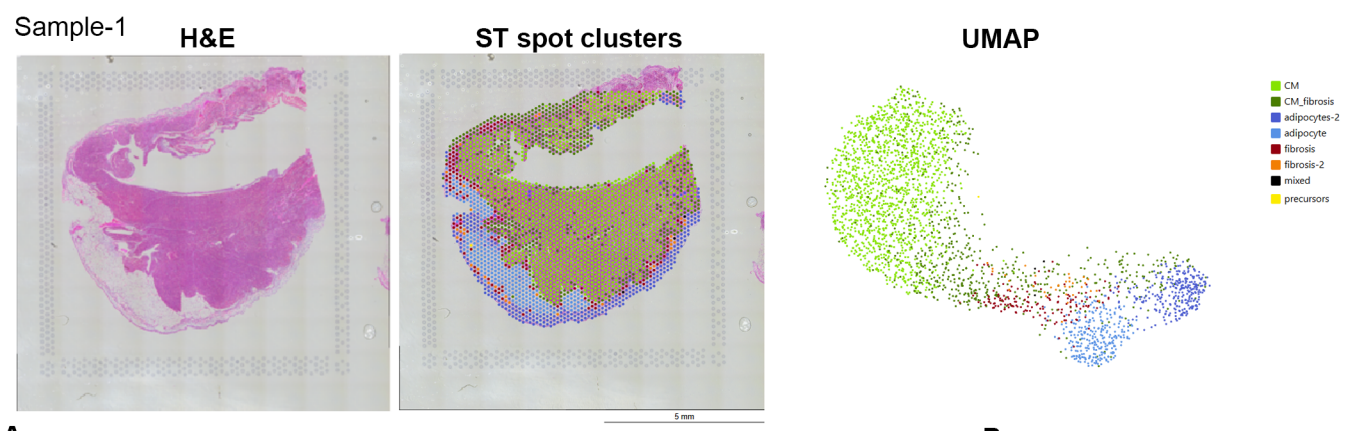

fig. S6 Spatial transcriptomic of human atrial specimen #1. Five-µm section of human atrial tissue after H&E staining (left) associated with spot plot clusters identified using Seurat based on specific gene expression. Uniform manifold approximation and projection (UMAP) clustering with Seurat showing gene expression patterns. (**A-F**) UMAP clustering with Seurat showing gene expression patterns for human atrial specimens merged asociated to spatial localization showing differential transcriptional signatures of adipocytes with the expression of FABP4 and perilipin-1 (PLIN1) (**A**), cardiomyocytes with the expression of MYH6 and NPPA (**B**), fibrosis with the expression of fibronectin (FBN) and collagen-1 (COL1A1) (**C**), macrophages with the expression of LYVE1 and CCL2 (**D**), epicardial progenitor cells (EPC) with the gene expression DNAJB1 and FOSB (**E**) and immune cells with the gene expression THY1 and CD34 (**F**).

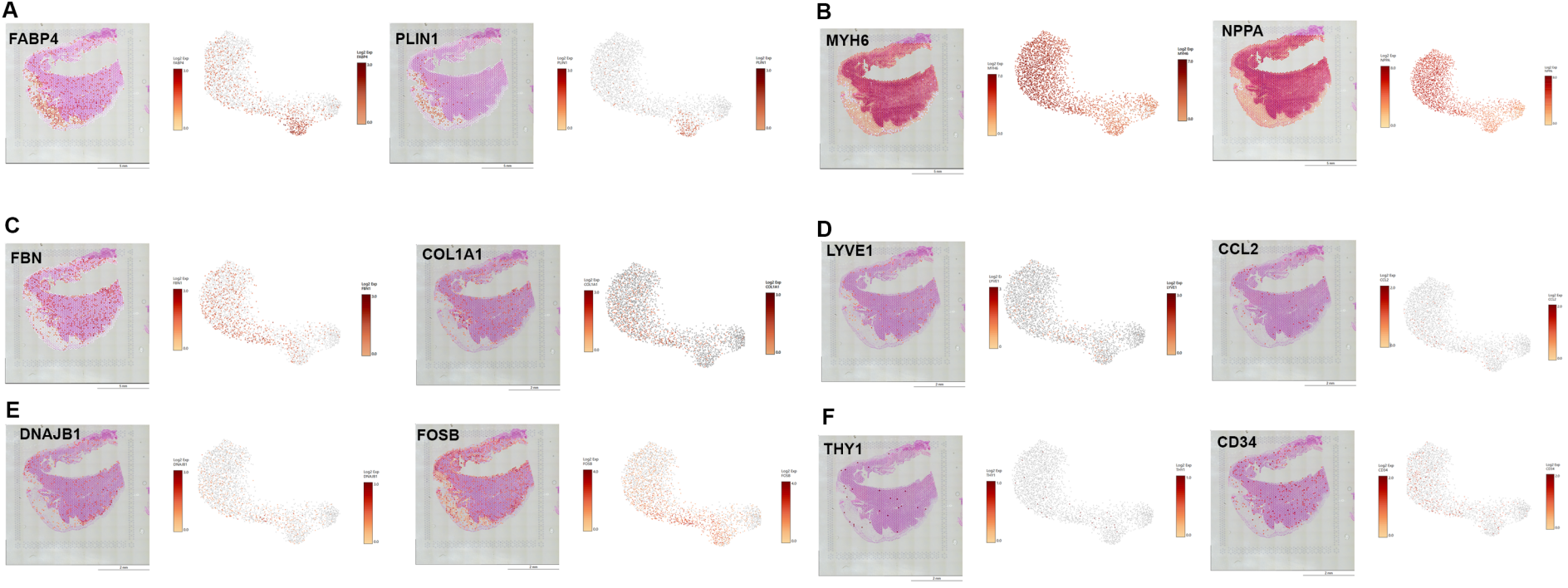

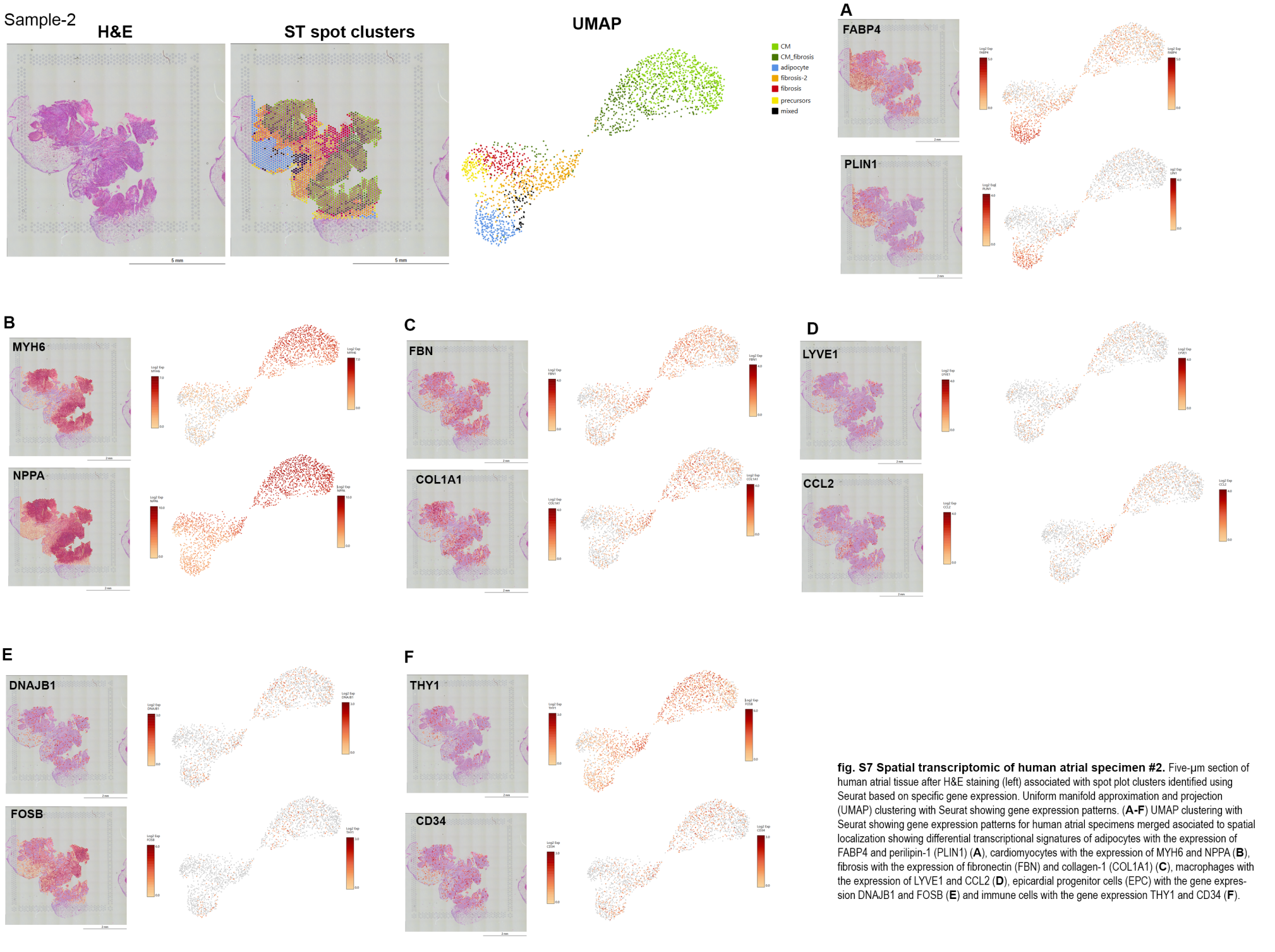

fig. S7 Spatial transcriptomic of human atrial specimen #2. Five-µm section of human atrial tissue after H&E staining (left) associated with spot plot clusters identified using Seurat based on specific gene expression. Uniform manifold approximation and projection (UMAP) clustering with Seurat showing gene expression patterns. (**A-F**) UMAP clustering with Seurat showing gene expression patterns for human atrial specimens merged asociated to spatial localization showing differential transcriptional signatures of adipocytes with the expression of FABP4 and perilipin-1 (PLIN1) (**A**), cardiomyocytes with the expression of MYH6 and NPPA (**B**), fibrosis with the expression of fibronectin (FBN) and collagen-1 (COL1A1) (**C**), macrophages with the expression of LYVE1 and CCL2 (**D**), epicardial progenitor cells (EPC) with the gene expression DNAJB1 and FOSB (**E**) and immune cells with the gene expression THY1 and CD34 (**F**).

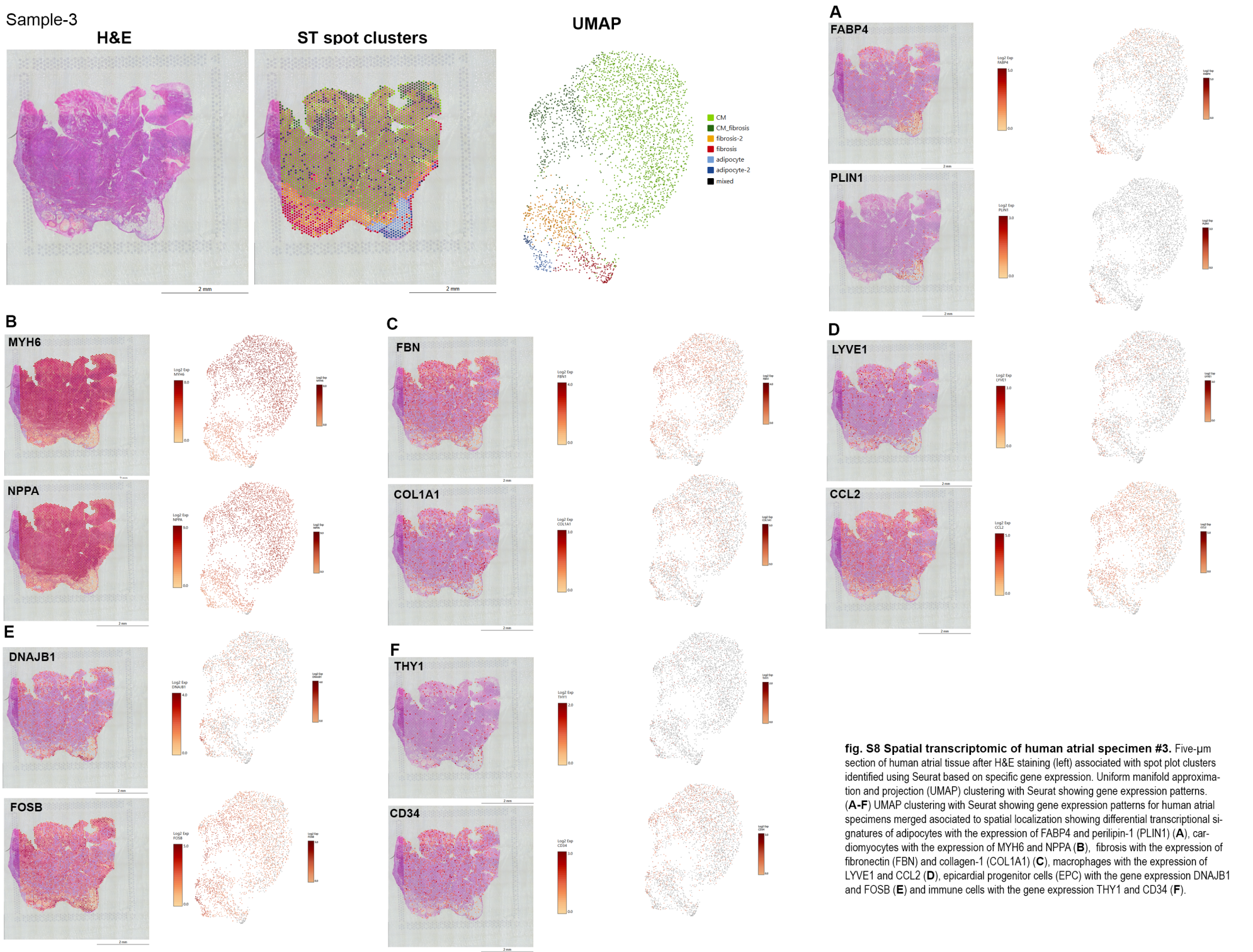

fig. S8 Spatial transcriptomic of human atrial specimen #3. Five-µm section of human atrial tissue after H&E staining (left) associated with spot plot clusters identified using Seurat based on specific gene expression. Uniform manifold approximation and projection (UMAP) clustering with Seurat showing gene expression patterns. (**A-F**) UMAP clustering with Seurat showing gene expression patterns for human atrial specimens merged asociated to spatial localization showing differential transcriptional signatures of adipocytes with the expression of FABP4 and perilipin-1 (PLIN1) (**A**), cardiomyocytes with the expression of MYH6 and NPPA (**B**), fibrosis with the expression of fibronectin (FBN) and collagen-1 (COL1A1) (**C**), macrophages with the expression of LYVE1 and CCL2 (**D**), epicardial progenitor cells (EPC) with the gene expression DNAJB1 and FOSB (**E**) and immune cells with the gene expression THY1 and CD34 (**F**).

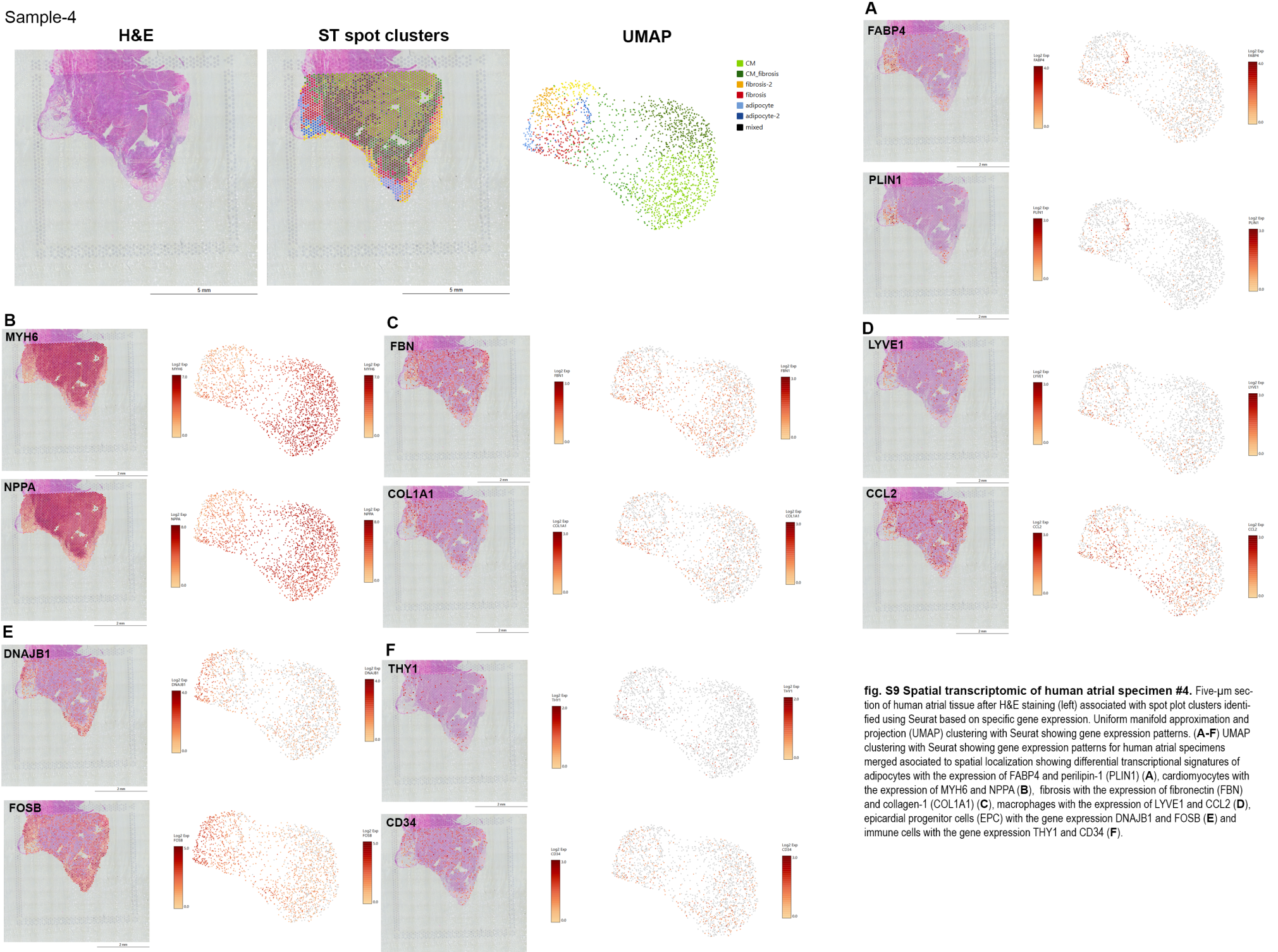

fig. S9 Spatial transcriptomic of human atrial specimen #4. Five-µm section of human atrial tissue after H&E staining (left) associated with spot plot clusters identified using Seurat based on specific gene expression. Uniform manifold approximation and projection (UMAP) clustering with Seurat showing gene expression patterns. (**A-F**) UMAP clustering with Seurat showing gene expression patterns for human atrial specimens merged asociated to spatial localization showing differential transcriptional signatures of adipocytes with the expression of FABP4 and perilipin-1 (PLIN1) (**A**), cardiomyocytes with the expression of MYH6 and NPPA (**B**), fibrosis with the expression of fibronectin (FBN) and collagen-1 (COL1A1) (**C**), macrophages with the expression of LYVE1 and CCL2 (**D**), epicardial progenitor cells (EPC) with the gene expression DNAJB1 and FOSB (**E**) and immune cells with the gene expression THY1 and CD34 (**F**).

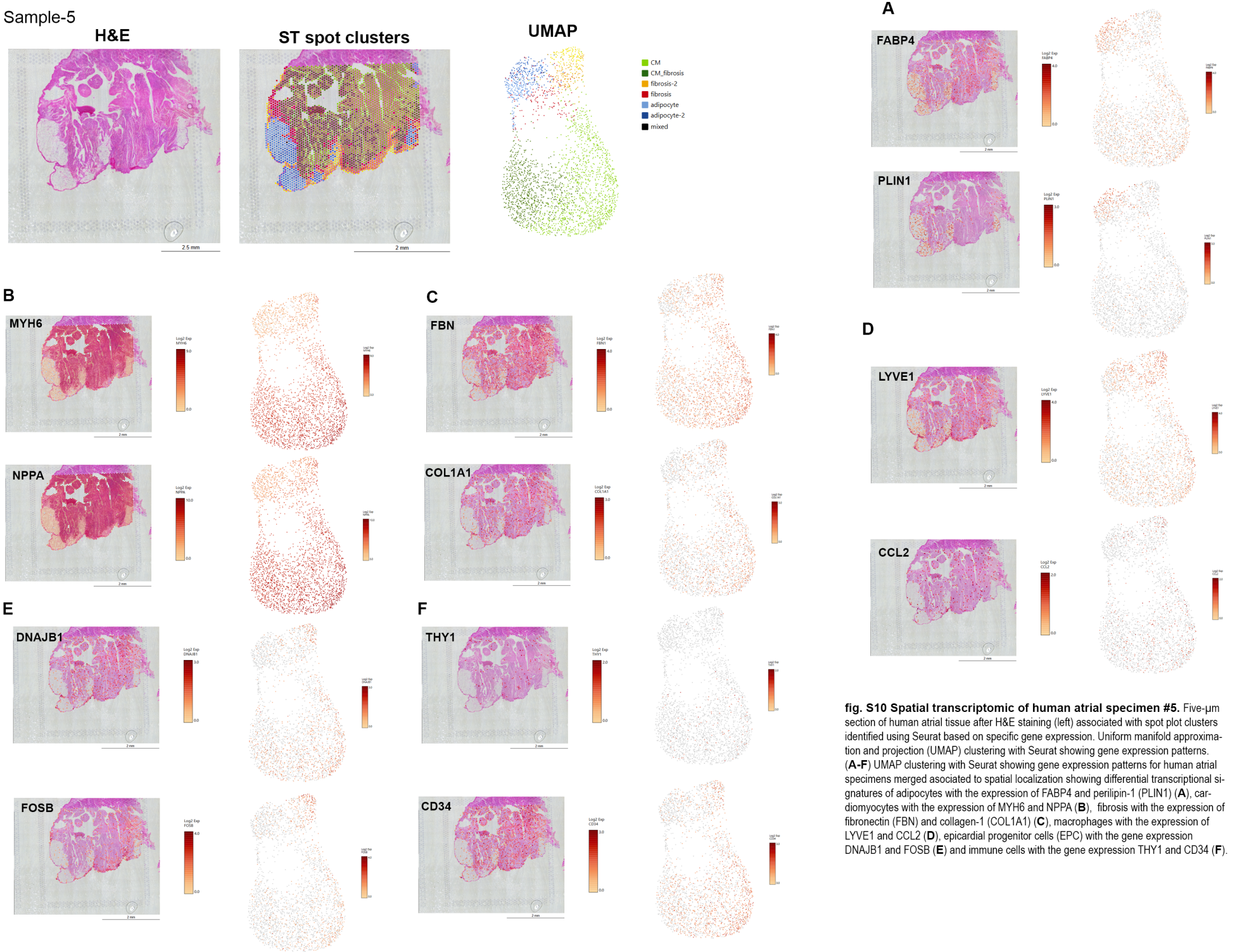

fig. S10 Spatial transcriptomic of human atrial specimen #5. Five-µm section of human atrial tissue after H&E staining (left) associated with spot plot clusters identified using Seurat based on specific gene expression. Uniform manifold approximation and projection (UMAP) clustering with Seurat showing gene expression patterns. (**A-F**) UMAP clustering with Seurat showing gene expression patterns for human atrial specimens merged associated to spatial localization showing differential transcriptional signatures of adipocytes with the expression of FABP4 and perilipin-1 (PLIN1) (**A**), cardiomyocytes with the expression of MYH6 and NPPA (**B**), fibrosis with the expression of fibronectin (FBN) and collagen-1 (COL1A1) (**C**), macrophages with the expression of LYVE1 and CCL2 (**D**), epicardial progenitor cells (EPC) with the gene expression DNAJB1 and FOSB (**E**) and immune cells with the gene expression THY1 and CD34 (**F**).

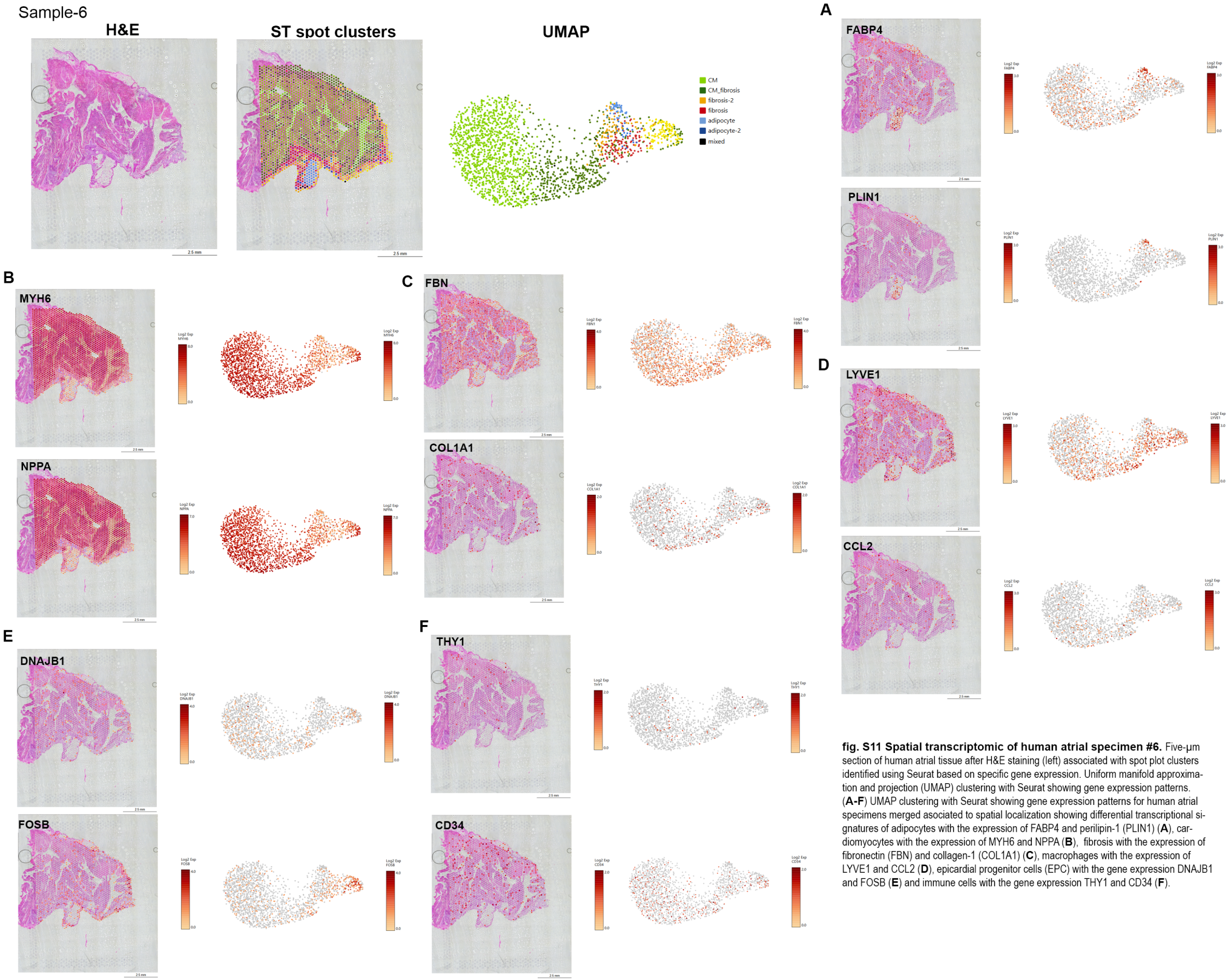

fig. S11 Spatial transcriptomic of human atrial specimen #6. Five-μm section of human atrial tissue after H&E staining (left) associated with spot plot clusters identified using Seurat based on specific gene expression. Uniform manifold approximation and projection (UMAP) clustering with Seurat showing gene expression patterns. (**A-F**) UMAP clustering with Seurat showing gene expression patterns for human atrial specimens merged asociated to spatial localization showing differential transcriptional signatures of adipocytes with the expression of FABP4 and perilipin-1 (PLIN1) (**A**), cardiomyocytes with the expression of MYH6 and NPPA (**B**), fibrosis with the expression of fibronectin (FBN) and collagen-1 (COL1A1) (**C**), macrophages with the expression of LYVE1 and CCL2 (**D**), epicardial progenitor cells (EPC) with the gene expression DNAJB1 and FOSB (**E**) and immune cells with the gene expression THY1 and CD34 (**F**).

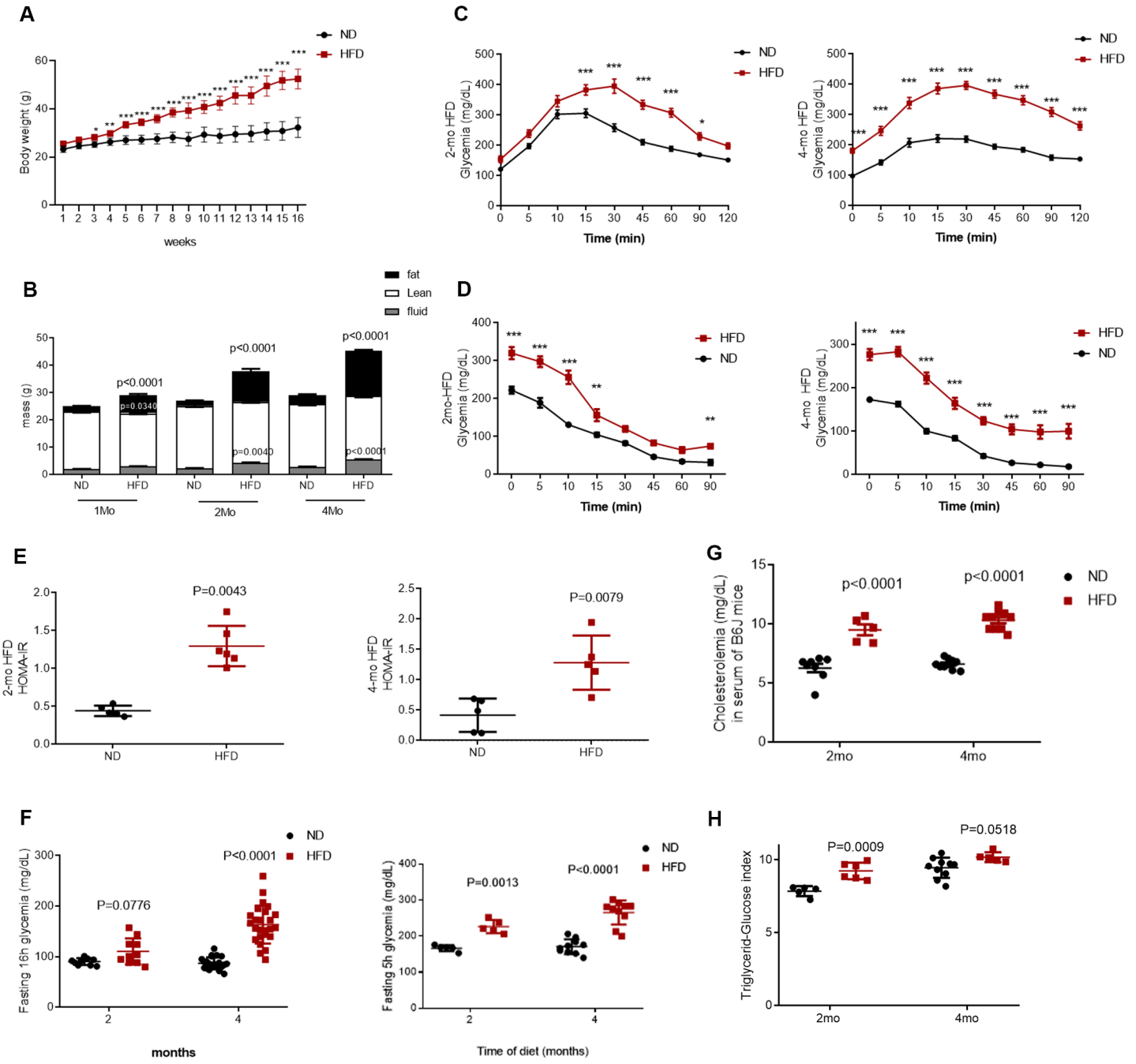

fig. S12 Metabolic syndromes progression in obese mice. (**A**, **B**) Body weight gain (**A**) and fat mass (**B**) of mice fed with high fat diet (HFD) for 1, 2 and 4 months. (**C**, **D**) ITT and OGTT measures of mice fed with HFD for 2 and 4 months (n=10-15). (**E**) HOMA-IR of mice fed with HFD for 2 and 4 months (n=6). (**F**) Glycemia measures for mice fasting for 16 hours or 5 hours after 2 and 4 months of HFD (n=10-15). (**H**) Triglyceride-glucose index (TGI) showing insulin-resistance of mice fed with HFD for 2 and 4 months (n=6-10). Data are presented as the mean ± standard deviation (SD) of three independent experiments and were analyzed using a one-way ANOVA followed by a Bonferroni's post-hoc test.

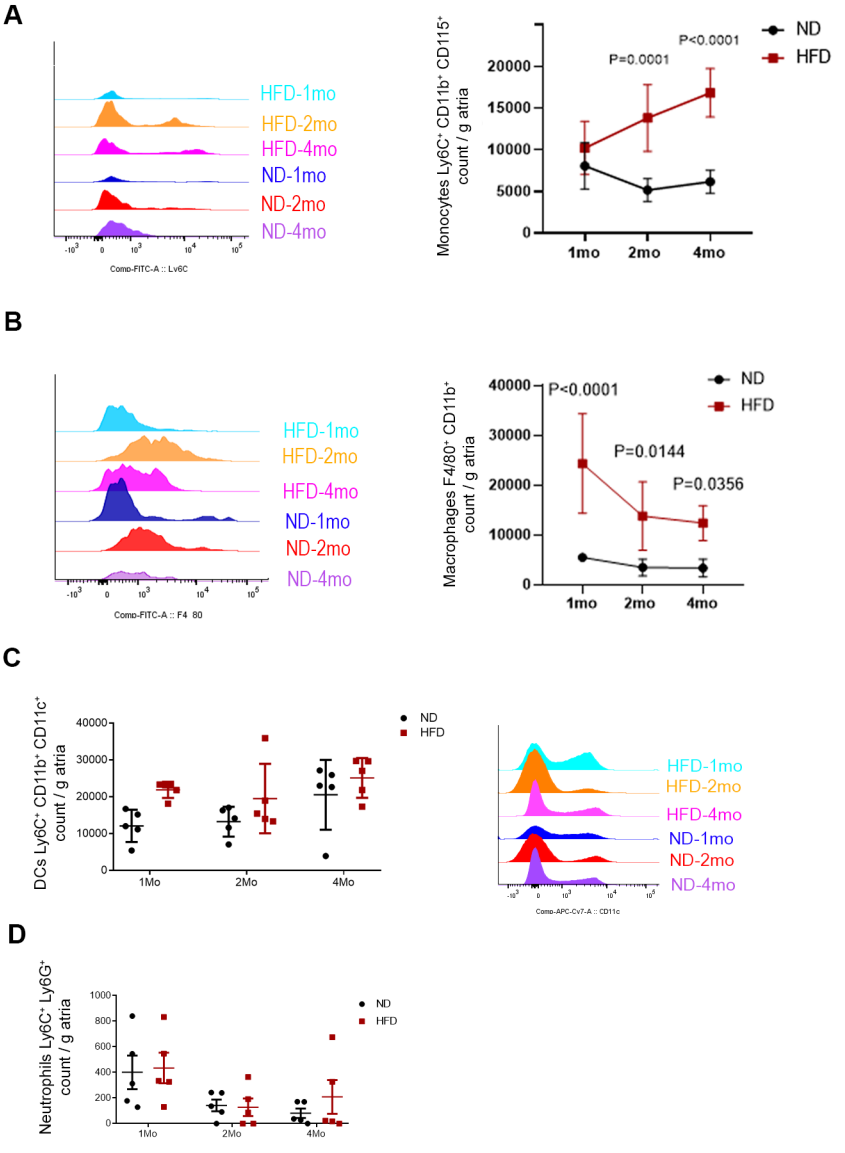

fig. S13 Macrophages recruitment during the progression of the atrial remodeling. (**A**, **B**) Flow cytometry half offset and histograms representing the quantification of Ly6C$^+$, CD11b$^+$, CD115$^+$ monocytes (**A**) and F4/80$^+$, CD11b$^+$ macrophages (**B**), Ly6C$^+$ CD11b$^+$ CD11c$^+$ dendritic cells (DCs) (**C**) and Ly6C$^+$ Ly6G$^+$ neutrophils (**D**) in the LA of obese and ND mice at 1, 2 and 4 months (mo). Data are presented as the mean ± standard deviation of three independent experiments and were analyzed using a one-way Anova followed by Bonferroni's post-hoc test.

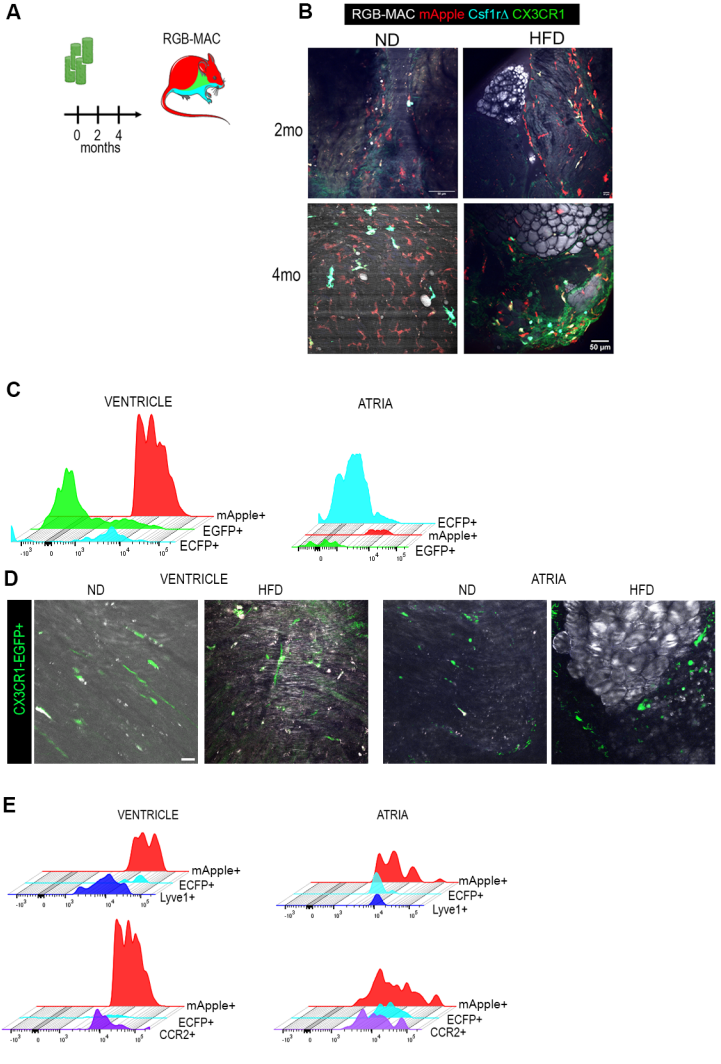

fig. S14 Myeloid cells infiltrated in obese mice atria. (**A-D**) Second harmonic generation (SHG) and coherent anti-stoke Raman spectroscopy (CARS) microscopy (**B**, **D**) of fresh LA of transgenic RGB-MAC mice (**A**) fed with HFD for 2 and 4 months showing the infiltration of mApple$^+$ and ECFP$^+$ cells into the adipose tissue (grey) and at the matrix (green) junction in the epicardial layer (n=4, each). Scale bar: 50 µm. (**C, E**) Flow cytometry half offset histograms representing the level expression of ECFP$^+$ mApple$^+$ Lyve1$^+$ and CCR2$^+$ in the left atrial (LA) and left ventricular cavities of obese RGB-MAC mice at 4 months (n=4, each).

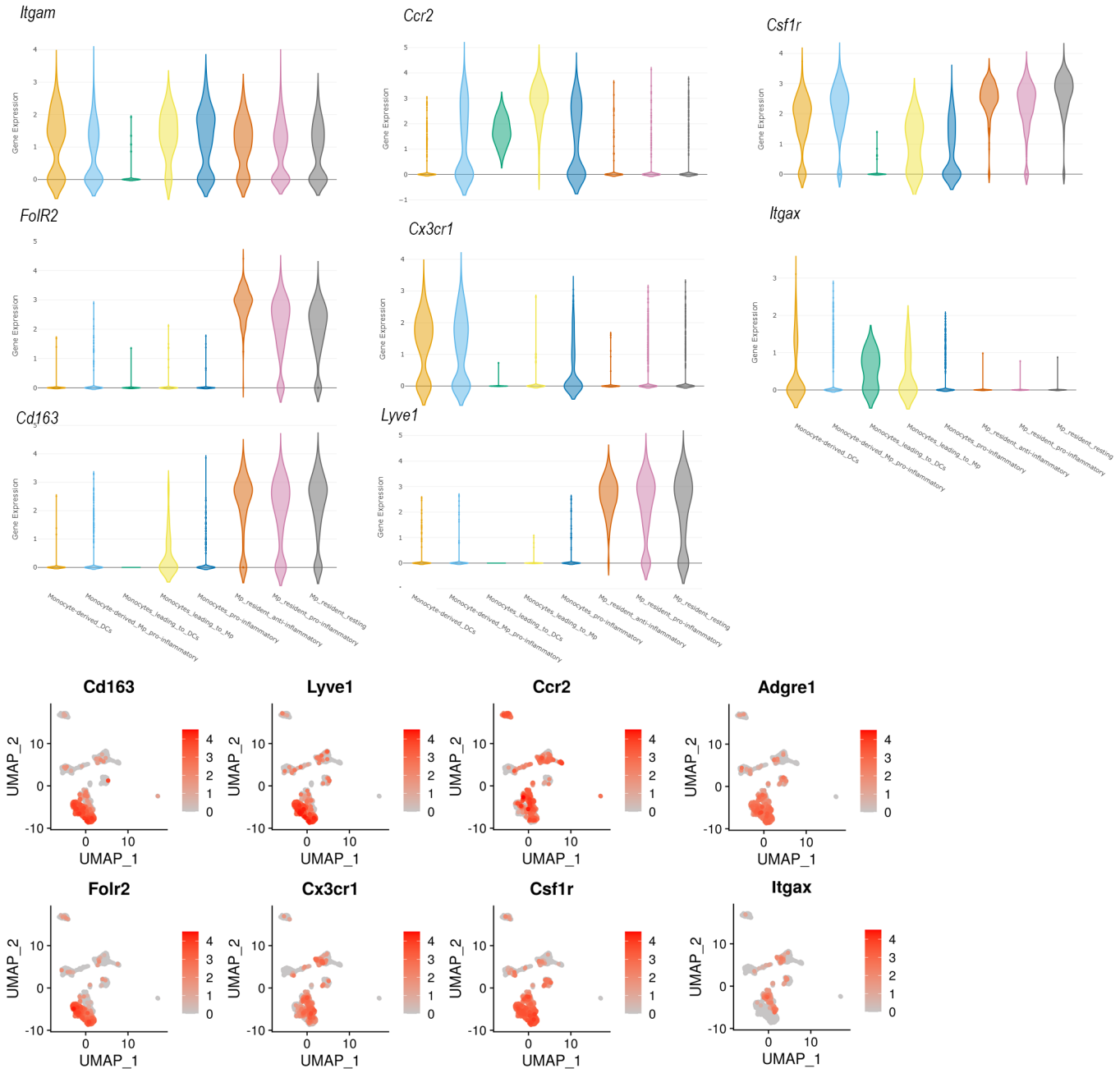

fig. S15 Single-cell RNA sequencing reveals macrophage subsets in the left atrium (LA) of obese mice. Violin plots showing the gene expression levels (normalized log-transformed values) according to the diet. Data were analyzed using a Kruskal-Wallis test followed by a two-sided Wilcoxon rank-sum test. Uniform manifold approximation and projection (UMAP) clustering with Seurat showing gene expression patterns for mouse atria showing differential transcriptional signatures of macrophages.

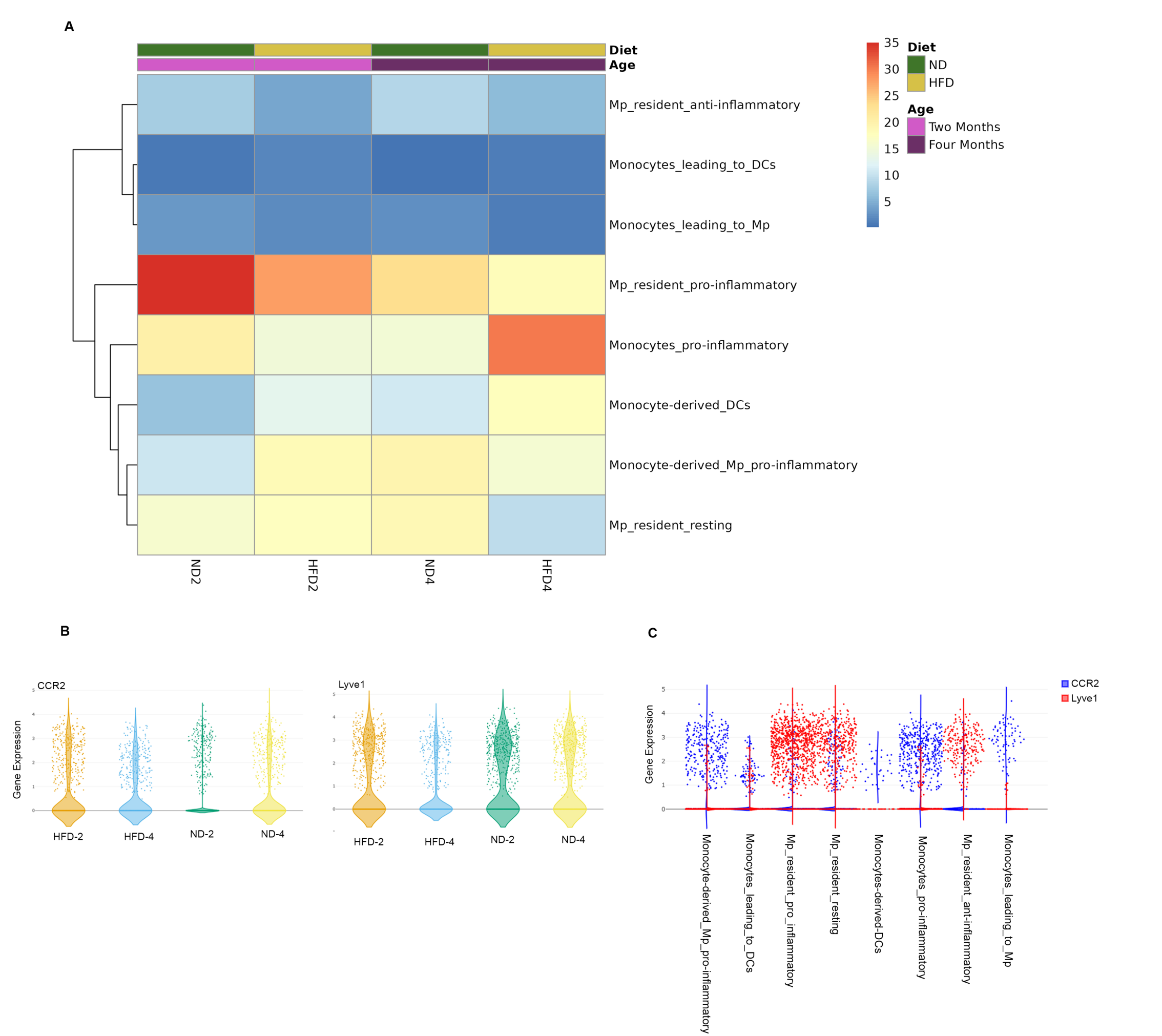

fig. S16 Single-cell RNA sequencing reveals macrophage subsets in the left atria (LA) of obese micel. (**A**) Heat map showing the differential expression of 15 top genes in the LA of obese and ND mice at 2 and 4 months. Color intensity of scale bar represents average expression of a given gene in a given cluster and was statistically significant ($p < 0.05$). (**B**) Violin plots showing the gene expression levels (normalized log-transformed values) according to the diet. Data were analyzed using a Kruskal-Wallis test followed by a two-sided Wilcoxon rank-sum test. (**C**) Violin plots showing the gene expression levels (normalized log-transformed values) according to the myeloid cluster. Data were analyzed using a Kruskal-Wallis test followed by a two-sided Wilcoxon rank-sum test.

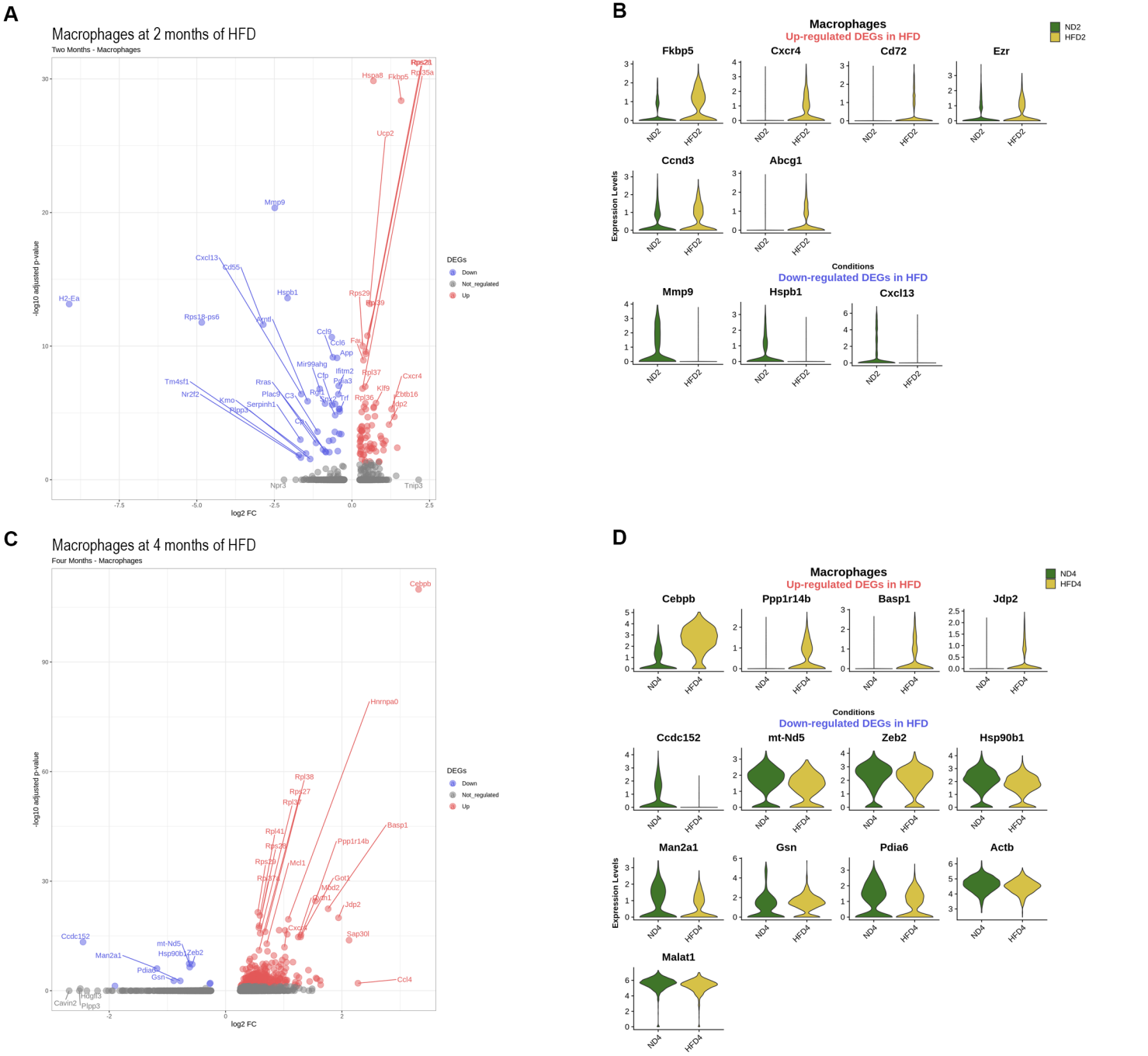

fig. S17 Obesity alters phenotype of macrophages in mice atria. (**A**,**C**) Volcano plot for DEGs; red colour highlights upregulated genes and blue colour represents downregulated genes in ND/HFD at 2 monts (**A**) and 4 months (**C**) of HFD (Padj < 0.05; two-sided Wald test with Benjamini–Hochberg adjustment) and |log2[fold change]| ≥ 1, and grey colour displays non-significant DEGs. (**B**, **D**) Violin plots showing the top gene expression levels (normalized log-transformed values) according to the diet at 2 months (**B**) and 4 months (**D**) of HFD.

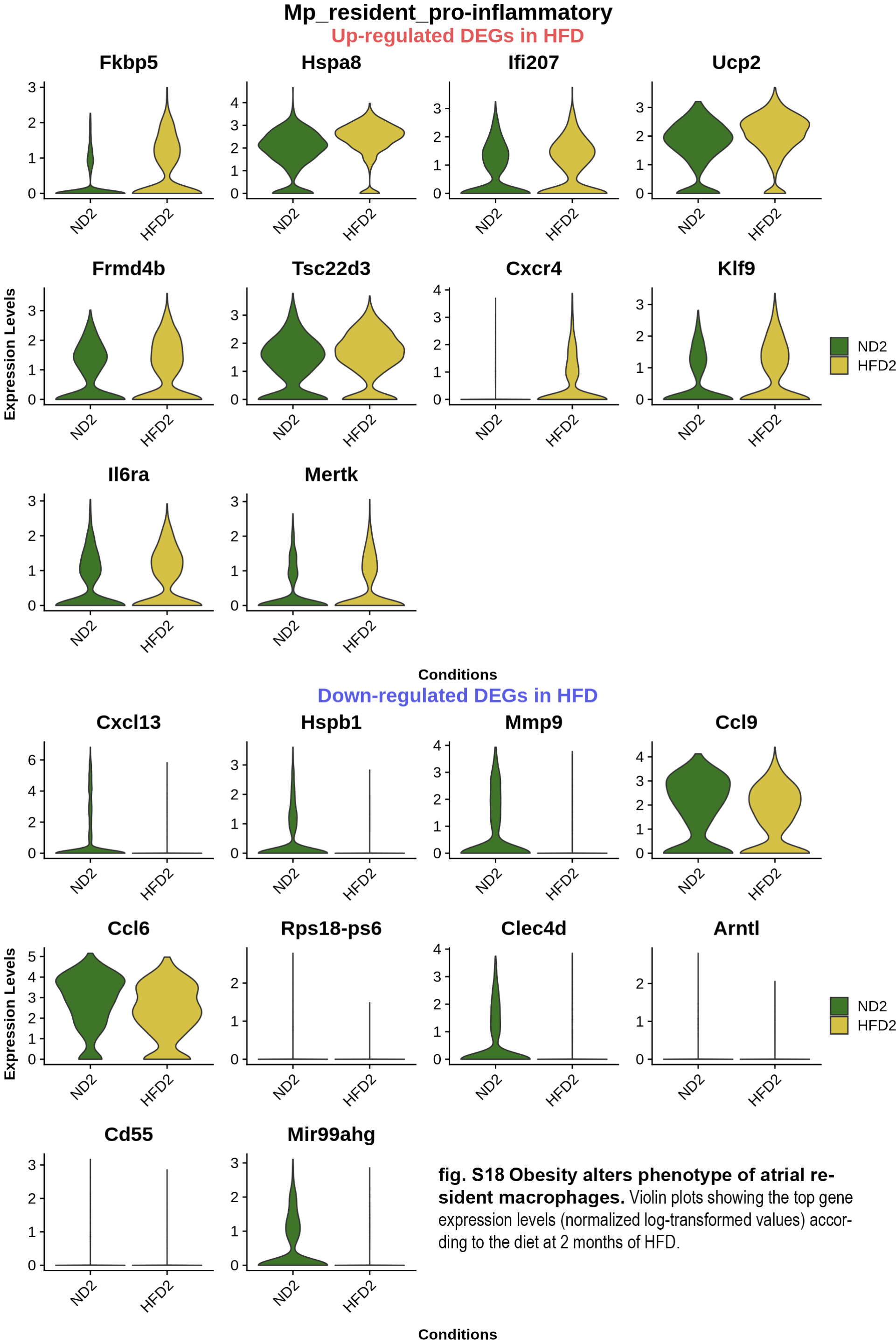

fig. S18 Obesity alters phenotype of atrial resident macrophages. Violin plots showing the top gene expression levels (normalized log-transformed values) according to the diet at 2 months of HFD.

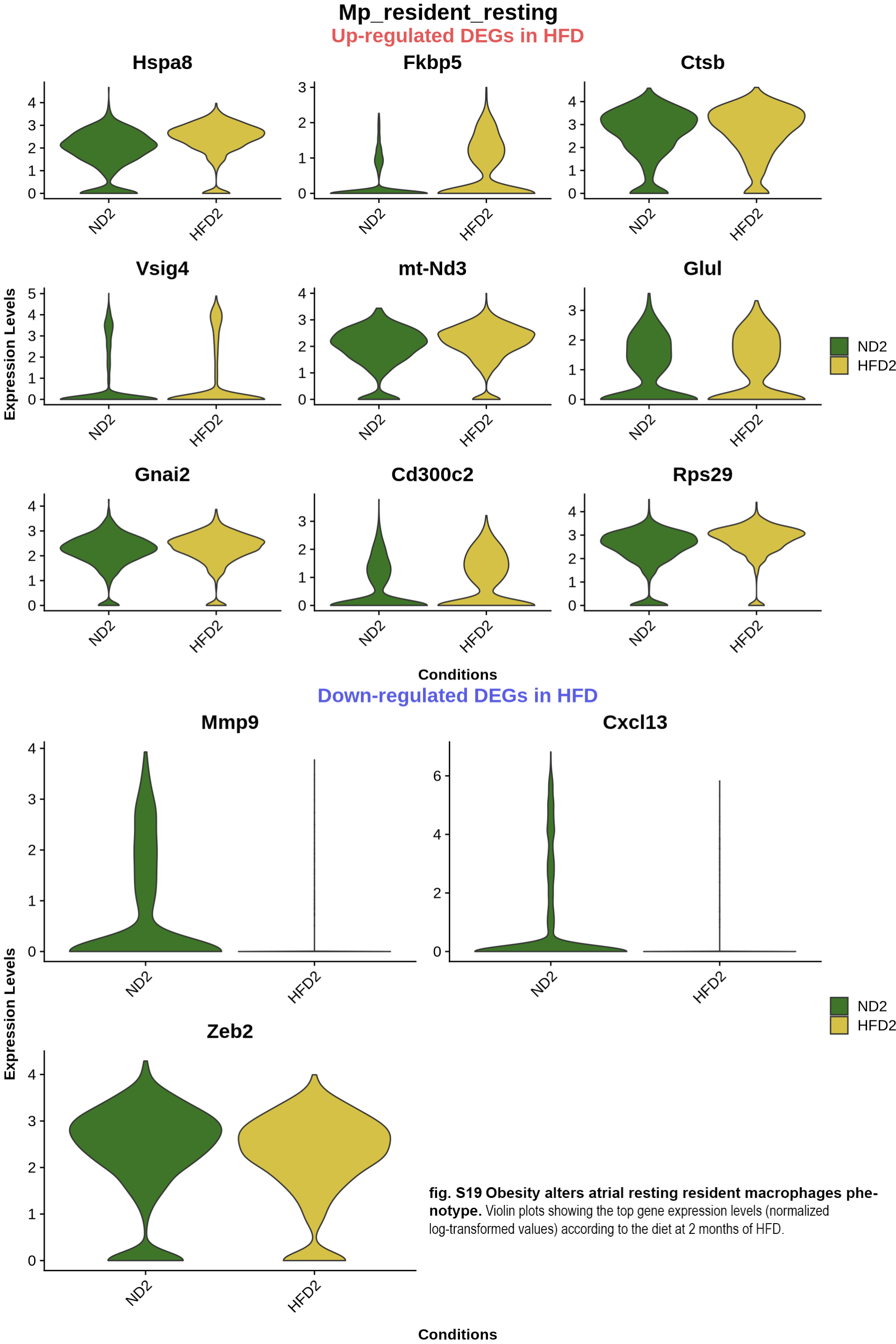

fig. S19 Obesity alters atrial resting resident macrophages phenotype. Violin plots showing the top gene expression levels (normalized log-transformed values) according to the diet at 2 months of HFD.

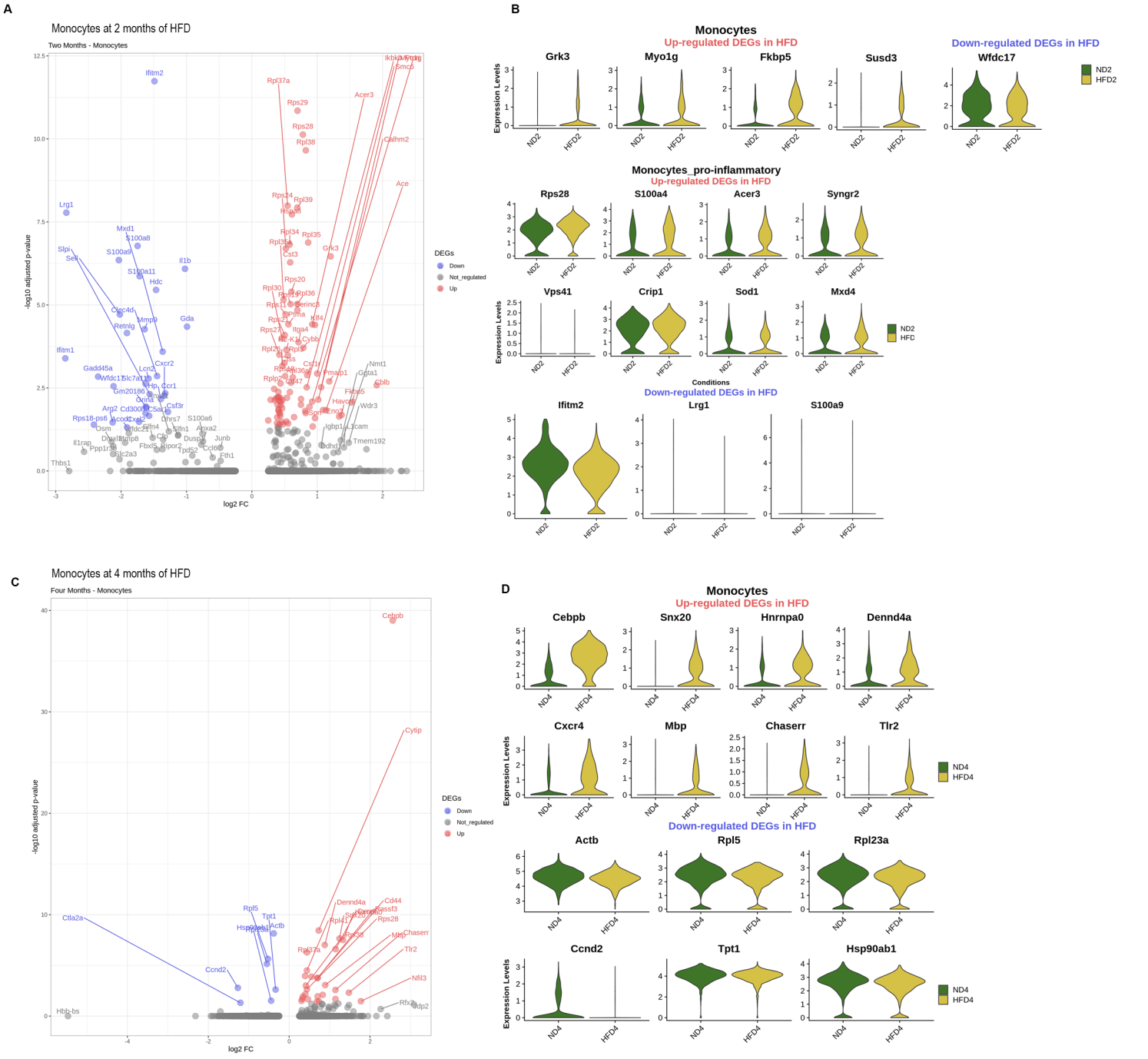

fig. S20 Obesity alters atrial monocytes phenotype. (**A**,**C**) Volcano plot for DEGs; red colour highlights upregulated genes and blue colour represents downregulated genes in ND/HFD at 2 monts (**A**) and 4 months (**C**) of HFD (Padj < 0.05; two-sided Wald test with Benjamini–Hochberg adjustment) and |log2[fold change]| ≥ 1, and grey colour displays non-significant DEGs. (B, D) Violin plots showing the top gene expression levels (normalized log-transformed values) according to the diet at 2 months (**B**) and 4 months (**D**) of HFD.

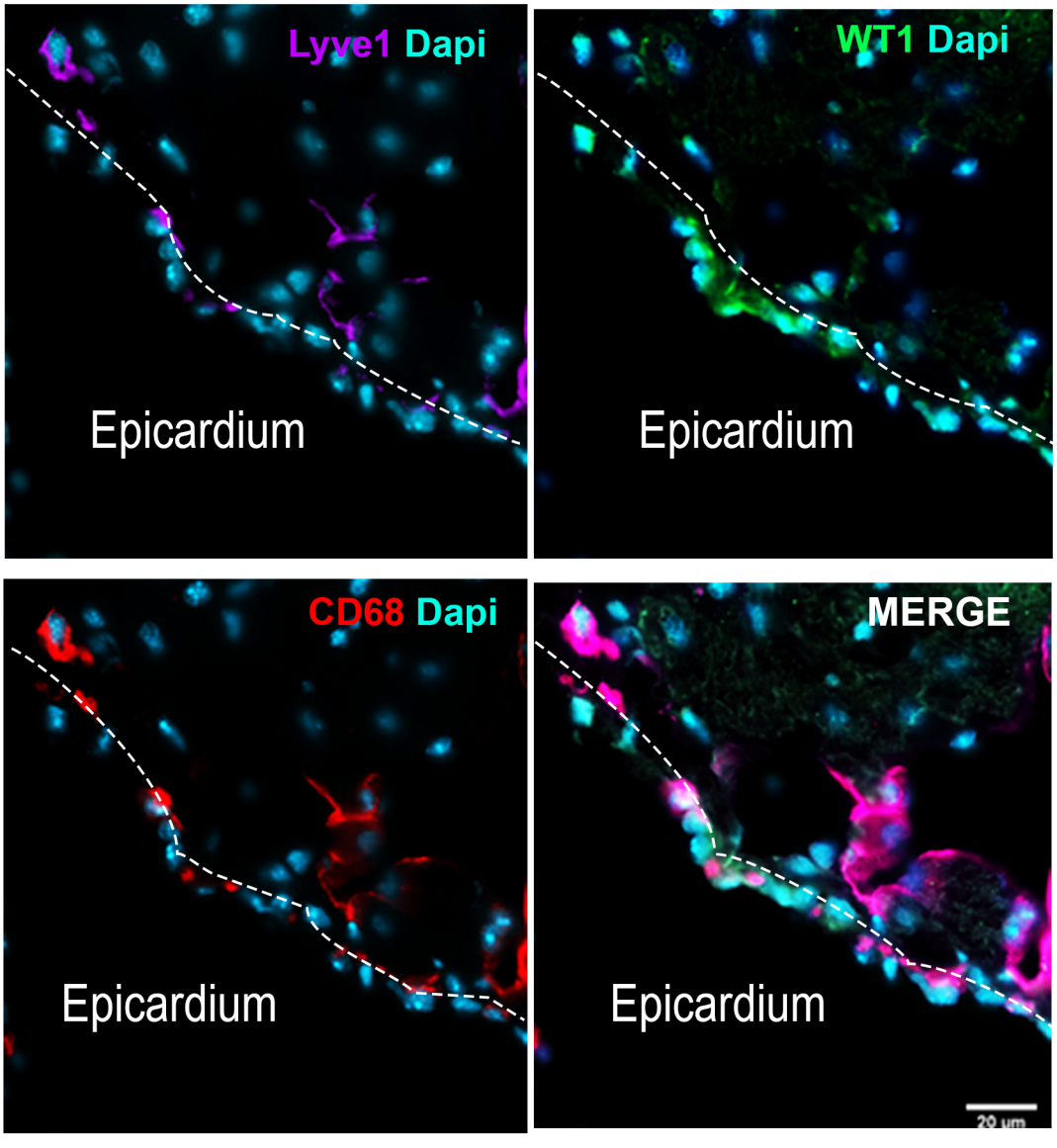

fig. S21 Close proximity between resident macorphages Lyve1⁺ and epicardial progenitor cells (EPC). Co-immunostaining with anti-Lyve1 antibody showing Lyve1⁺ macrophages in the epicardial layer and myocardium of the LA control-ND mice (n=4, each). Scale bar: 5 µm.

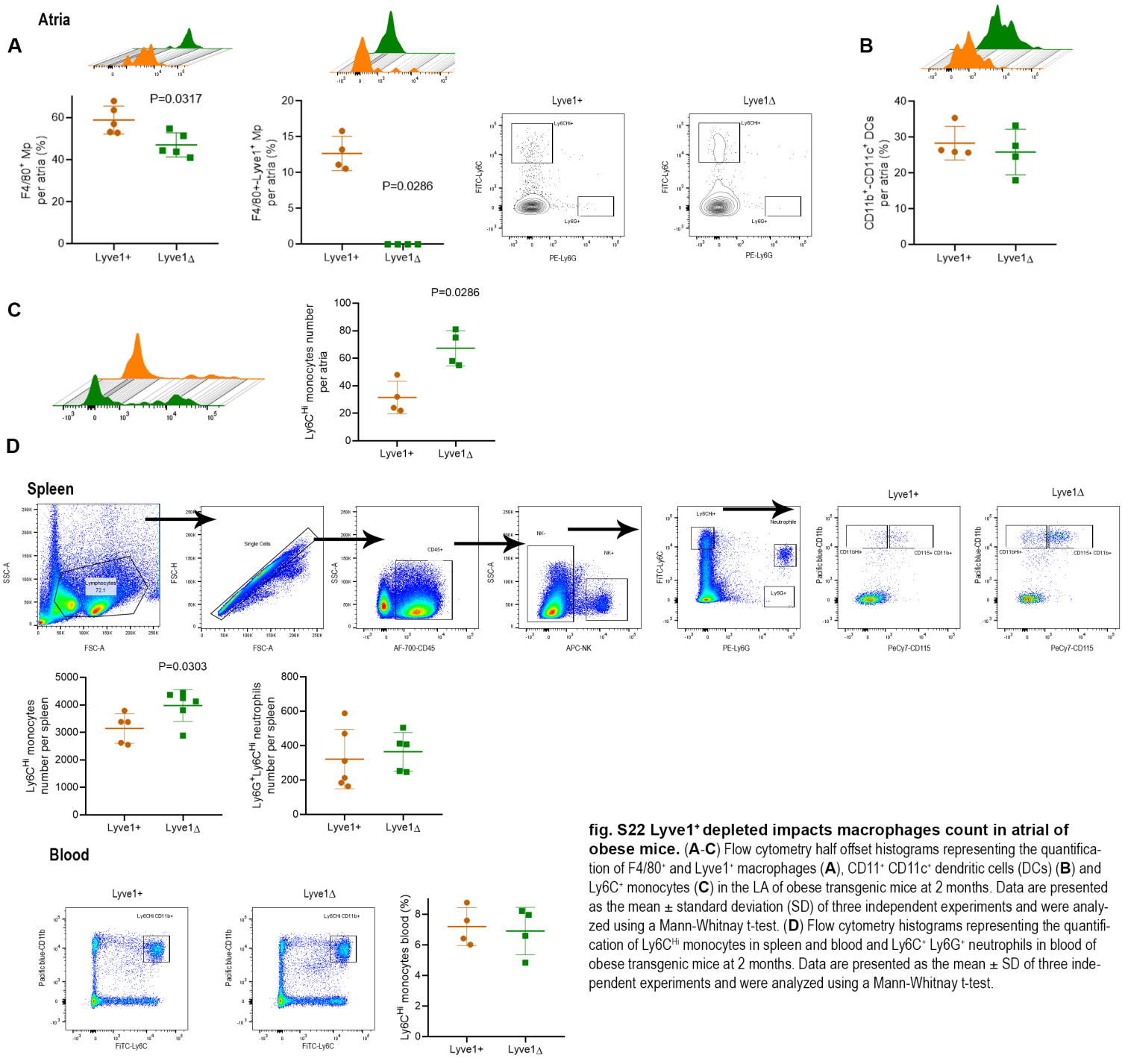

fig. S22 Lyve1⁺ depleted impacts macrophages count in atrial of obese mice. (**A**-**C**) Flow cytometry half offset histograms representing the quantification of F4/80⁺ and Lyve1⁺ macrophages (**A**), CD11⁺ CD11c⁺ dendritic cells (DCs) (**B**) and Ly6C⁺ monocytes (**C**) in the LA of obese transgenic mice at 2 months. Data are presented as the mean ± standard deviation (SD) of three independent experiments and were analyzed using a Mann-Whitnay t-test. (**D**) Flow cytometry histograms representing the quantification of Ly6C^{Hi} monocytes in spleen and blood and Ly6C⁺ Ly6G⁺ neutrophils in blood of obese transgenic mice at 2 months. Data are presented as the mean ± SD of three independent experiments and were analyzed using a Mann-Whitnay t-test.

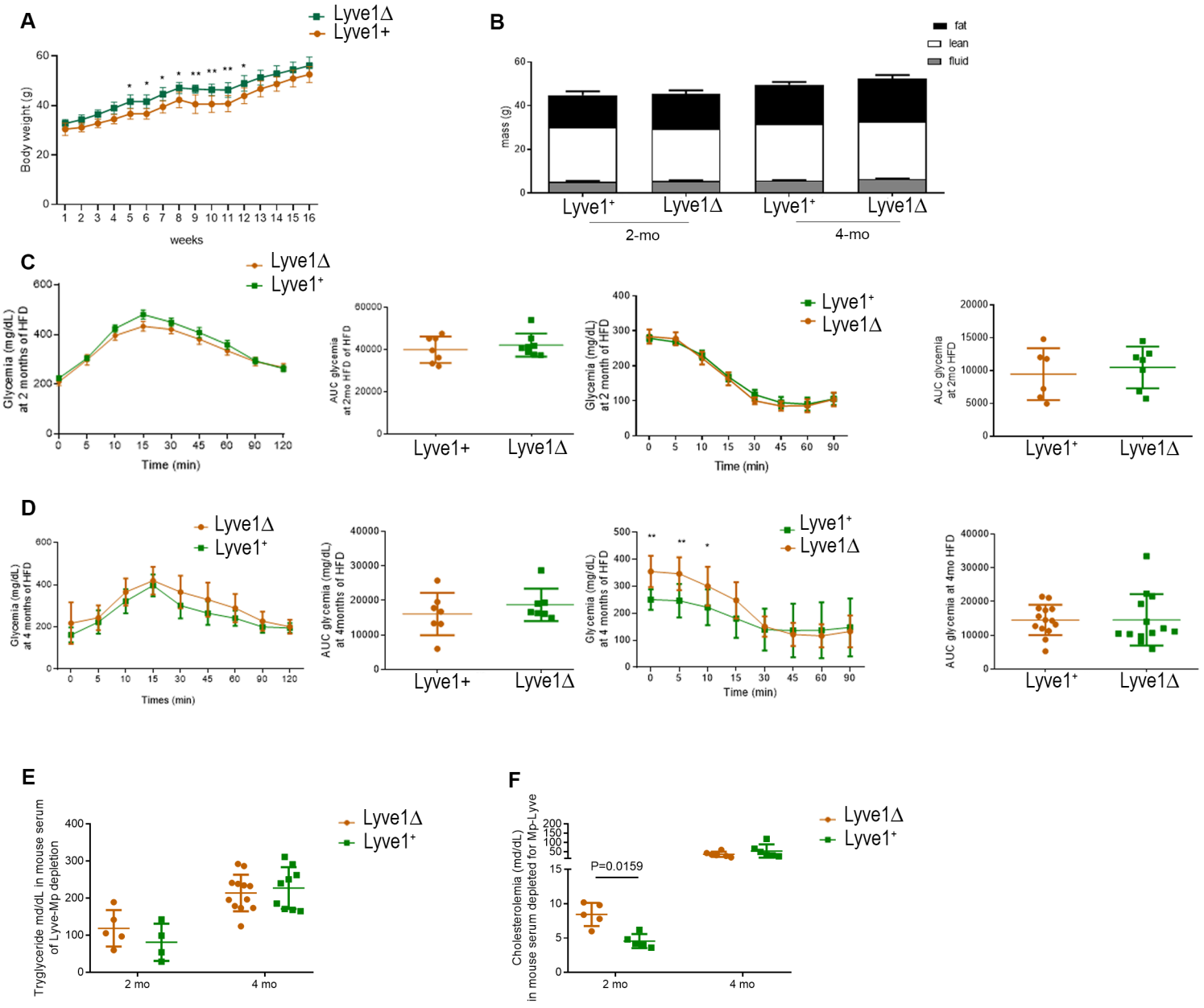

fig. S23 Metabolic syndrome of Lyve1 resident macrophages depleted in obese mice. Body weight gain (**A**) and fat mass (**B**) of Lyve1Δ and Lyve1⁺ mice fed with high fat diet (HFD) for 2 and 4 months. (**C**, **D**) Measures of glycemia in ITT, OGTT and AUC level of fasting mice for 16 and 5 hours of Lyve1Δ and Lyve1⁺ mice fed with HFD for 2 (**C**) and 4 (**D**) months (n=6-15). (**E**, **F**) Triglyceride (**E**) and cholesterol (**F**) level were measured in blood of fasting mice for 16 hours of Lyve1Δ and Lyve1⁺ mice after 2 and 4 months of HFD (n=6-10). Data are presented as the mean ± standard deviation of three independent experiments and were analyzed using a one-way ANOVA followed by a Bonferroni's post-hoc test and a Mann–Whitney test (histograms **C**,**D**).

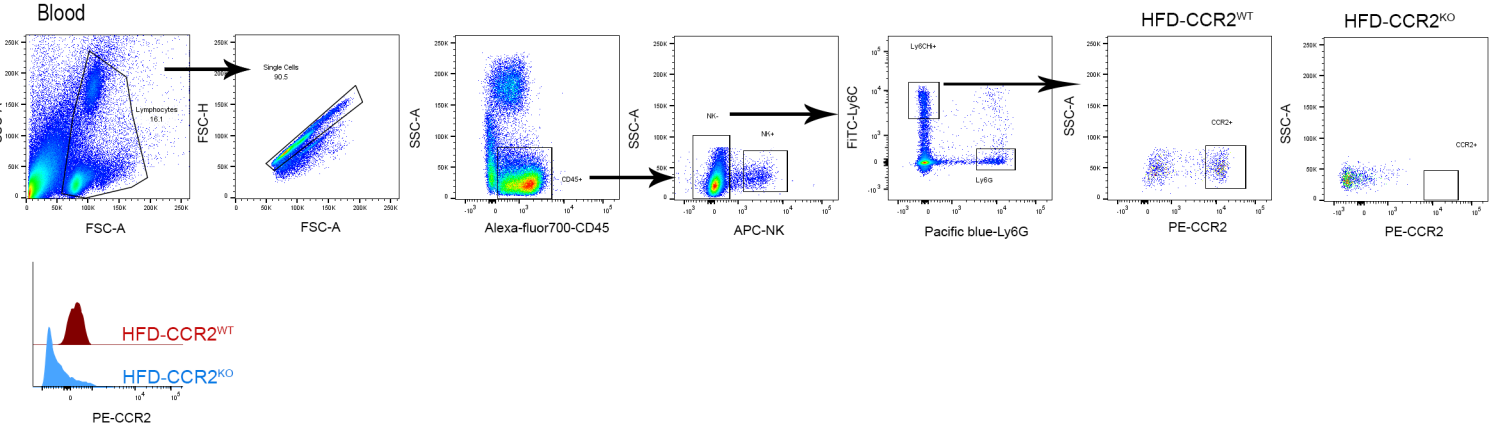

fig. S24 Monocytes depleted in transgenic mice CCR2^{KO}. Flow cytometry half offset histograms representing the quantification of Ly6C+, Ly6G^{+}, CCR2^{+} in blood of obese CCR2^{WT} and CCR2^{KO} mice at 2 months. Data are the mean ± standard deviation of three independent experiments and were analyzed using a Mann–Whitney test.

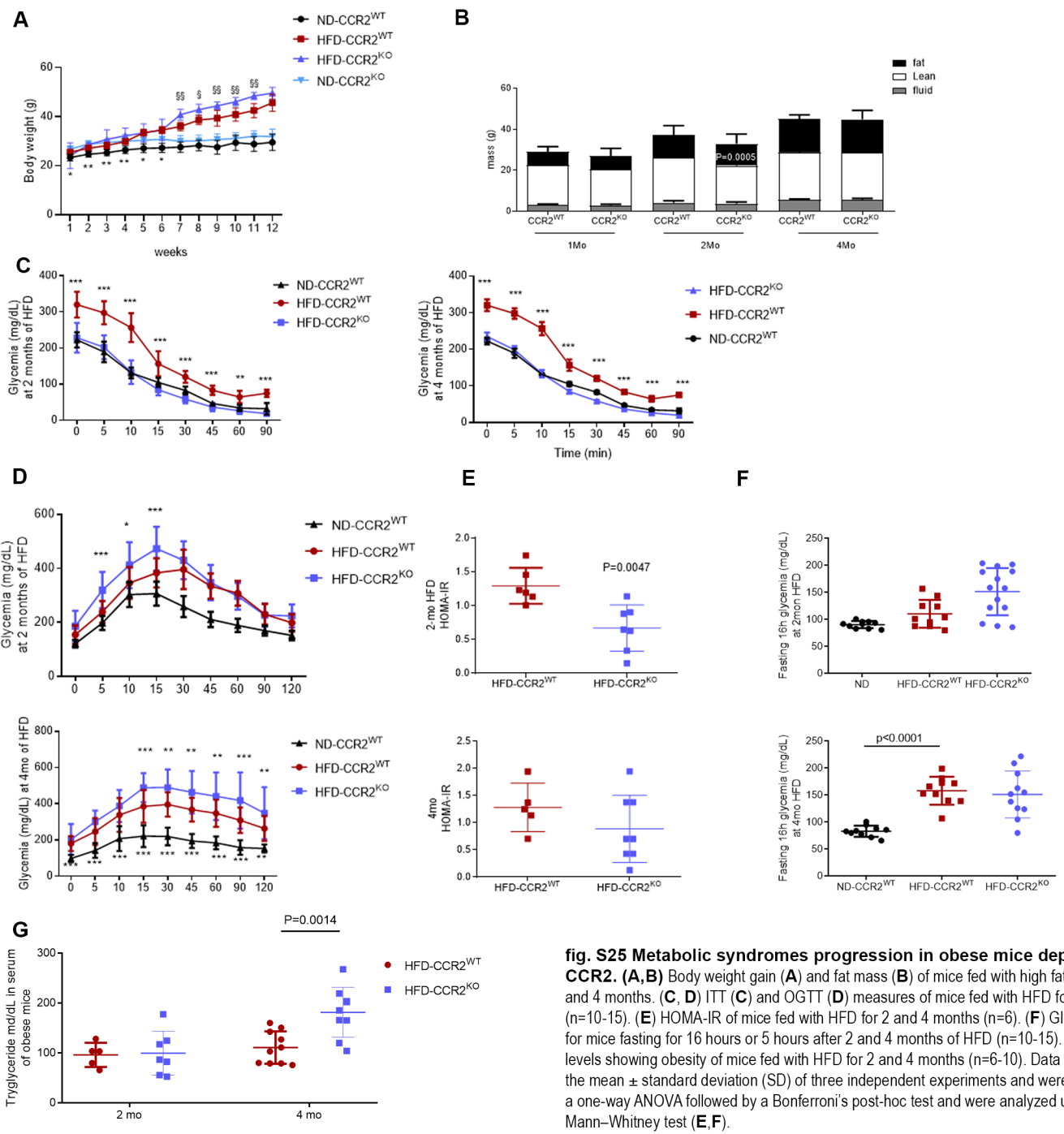

fig. S25 Metabolic syndromes progression in obese mice depleted in CCR2. (A,B) Body weight gain (**A**) and fat mass (**B**) of mice fed with high fat diet (HFD) for 2 and 4 months. (**C**, **D**) ITT (**C**) and OGTT (**D**) measures of mice fed with HFD for 2 and 4 months (n=10-15). (**E**) HOMA-IR of mice fed with HFD for 2 and 4 months (n=6). (**F**) Glycemia measures for mice fasting for 16 hours or 5 hours after 2 and 4 months of HFD (n=10-15). (**G**) Triglyceride levels showing obesity of mice fed with HFD for 2 and 4 months (n=6-10). Data are presented as the mean ± standard deviation (SD) of three independent experiments and were analyzed using a one-way ANOVA followed by a Bonferroni's post-hoc test and were analyzed using a Mann–Whitney test (**E**,**F**).

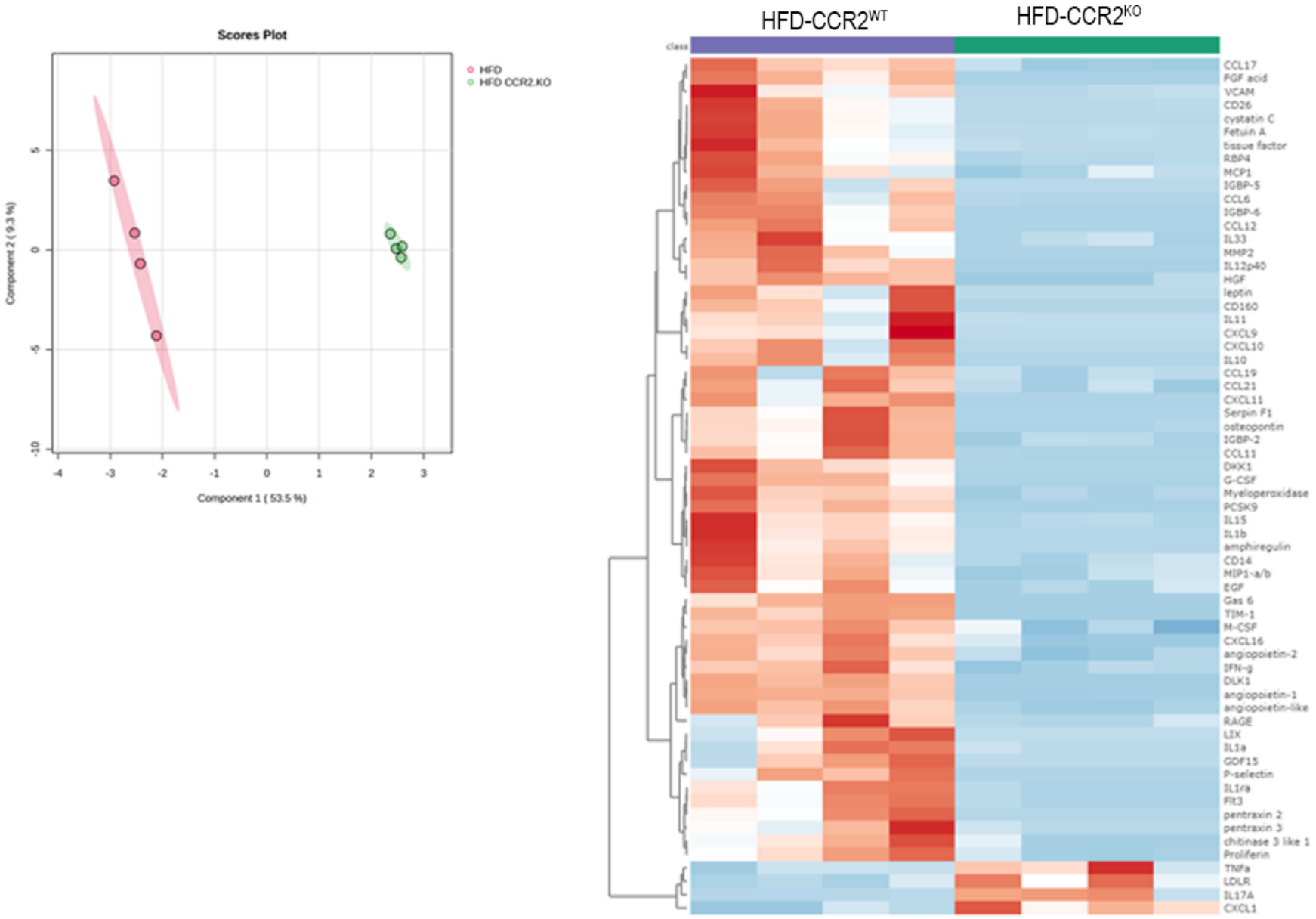

fig. S26 Inflammatory cytokines decrease in obese atria of CCR2^{KO} mice. Principal component analysis (PCA) (left) and heat map (right) representing the false discovery rates (FDR) (avg_log2FC) of cytokines detected in the LA of obese CCR2^{WT} and CCR2^{KO} mice at 2 months (n=4). Color intensity of scale bar represents average expression of a protein in a given cluster and was statistically significant ($p < 0.05$).